flaring plasma is associated only with the late-type star, and the binary nature of Algol is irrelevant, at least for this giant flare. The flare does, however, also display several features not observed in solar flares. Solar flares are never observed in polar regions; instead they are confined to the active region belt at lower heliographic latitudes. The thermal plasma in the giant flare on Algol is dominated by temperatures of 1×10^8 K; such temperatures are occasionally observed in solar flares[25,26] as 'super hot plasmas', but they contain only small fractions of the overall emission measure. The derived minimum plasma density is similar to the plasma densities of many solar flares[27], which would require a volume close to V_{max} to satisfy the observed energy budget. Higher densities with correspondingly smaller volumes can, of course, not be excluded; however, much higher densities quickly lead to implausibly large thermal pressures. Thus, the real challenge to theory is the construction of physically consistent reconnection-based flare models with the observed stellar parameters and clarify the effect of giant flares on the mass and angular momentum loss of active stars. □

Received 17 February; accepted 19 July 1999.

1. Kürster, M. & Schmitt, J. H. M. M. Forty days in the life of CF Tucanae (=HD 5303). The longest stellar X-ray flare observed with ROSAT. *Astron. Astrophys.* **311,** 211–229 (1996).
2. Foing, B. H. *et al.* in *IAU Colloq. 153: Magnetodynamic Phenomena in the Solar Atmosphere—Prototypes of Stellar Magnetic Activity* (eds Uchida, Y., Kosugi, T. & Hudson, H. S.) 283–284 (Kluwer Academic, Dordrecht, 1996).
3. Graffagnino, V. G., Wonnacott, D. & Schaeidt, S. HR 5110 superflare: an interbinary flare identified? *Mon. Not. R. Astron. Soc.* **275,** 129–142 (1995).
4. Ottmann, R. & Schmitt, J. H. M. M. ROSAT observation of a giant X-ray flare on Algol: evidence for abundance variations? *Astron. Astrophys.* **307,** 813–823 (1996).
5. Preibish, T., Zinnecker, H. & Schmitt, J. H. M. M. ROSAT-detection of a giant X-ray flare on LkH-α 92. *Astron. Astrophys.* **279,** L33–L366 (1993).
6. Preibisch, T., Neuhäuser, R. & Alcala, J. M. A giant X-ray flare on the young star P1724. *Astron. Astrophys.* **304,** L13–L16 (1996=5).
7. Grosso, N., Montmerle, T., Feigelson, E. D., Andre, P., Casanova, S. & Gregorio-Hetem, J. An X-ray superflare on an infrared protostar. *Nature* **387,** 56–58 (1997).
8. Ferreira, J. M. On the problem of very energetic flares in binary systems. *Astron. Astrophys.* **335,** 248–254 (1998).
9. Van den Oord, G. H. J. Filament support and flares in binaries. *Astron. Astrophys.* **205,** 167–180 (1988).
10. Schmitt, J. H. M. M., Fleming, T. A. & Giampapa, M. S. The X-ray view of the low-mass stars in the solar neighborhood. *Astrophys. J.* **450,** 392–400 (1995).
11. Schmitt, J. H. M. M. Coronae on solar-like stars. *Astron. Astrophys.* **318,** 215–230 (1997).
12. Forbes, T. G. in *Magnetic Reconnection in the Solar Atmosphere* (eds Bentley, R. D. & Mariska, J. T.) Vol. 111, 259–267 (ASP Conf. Ser., 1997).
13. Hudson, H. S. & Khan, J. I. in *Magnetic Reconnection in the Solar Atmosphere* (eds Bentley, R. D. & Mariska, J. T.) Vol. 111, 135–144 (ASP Conf. Ser., 1997).
14. Tsuneta, S. in *Magnetic Reconnection in the Solar Atmosphere* (eds Bentley, R. D. & Mariska, J. T.) Vol. 111, 409–418 (ASP Conf. Ser., 1997).
15. Al-Naimiy, H. M. K., Mutter, A. A. A. & Flaih, H. A. UBV photometry and light-curve analysis of Algol. *Astrophys. Space Sci.* **108,** 227–236 (1985).
16. Stern, R. A., Uchida, Y., Tsuneta, S. & Nagase, F. Ginga observations of X-ray flares on Algol. *Astrophys. J.* **400,** 321–329 (1992).
17. Van den Oord, G. H. J. & Mewe, R. The X-ray flare and the quiescent emission from Algol as detected by OXOSAT. *Astron. Astrophys.* **213,** 245–260 (1989).
18. White, N. E., Culhane, J. L., Parmar, A. N., Kellett, B. J., Kahn, S., Van den Oord, G. H. J. & Kuijpers, J. An EXOSAT observation of quiescent and flare coronal X-ray emission from Algol. *Astrophys. J.* **301,** 262–274 (1997).
19. Boella, G., Butler, R. C., Perola, G. C., Piro, L., Scarsi, L. & Bleeker, J. A. M. The medium-energy concentrator spectrometer on board the BeppoSAX X-ray astronomy satellite. *Astron. Astrophys.* (suppl.) **122,** 327–340 (1997).
20. Favata, F. & Schmitt, J. H. M. M. Spectroscopic analysis of a superhot giant flare observed on Algol by BeppoSAX. *Astron. Astrophys.* (accepted).
21. Tsuneta, S. Structure and dynamics of magnetic reconnection in a solar flare. *Astrophys. J.* **456,** 840–849 (1996).
22. Strassmeier, K. G. in *176th IAU Symp.* on Stellar Surface Structure (eds Strassmeier, K. G. & Linsky, J. L.) 289–298 (Kluwer Academic, Dordrecht, 1996).
23. Byrne, P. B. in *176th IAU Symp.* on Stellar Surface Structure (eds Strassmeier, K. G. & Linsky, J. L.) 299–303 (Kluwer Academic, Dordrecht, 1996).
24. Saar, S. H. in *IAU Colloq. 153: Magnetodynamic Phenomena in the Solar Atmosphere—Prototypes of Stellar Magnetic Activity* (eds Uchida, Y., Kosugi, T. & Hudson, H. S.) 367–374 (Kluwer Academic, Dordrecht, 1996).
25. Masuda, S., Kosugi, S., Hara, H., Tsuneta, S. & Ogawara, Y. A loop-top hard X-ray source in a compact solar flare as evidence for magnetic reconnection. *Nature* **371,** 495–497 (1994).
26. Hudson, H. S. & Nitta, N. in *High Energy Solar Physics* (eds Ramaty, R., Mandzhavidze, N. & Hua, X.-M.) **374,** 285–293 (AIP Conf. Proc., 1996).
27. Bray, R. J., Cram, L. E., Durrant, C. J. & Loughhead, R. E. Plasma loops in the solar corona. *Cambridge Astrophys. Ser.* **18,** 239 (1991).

Correspondence and requests for materials should be addressed to J.H.M.M.S. (e-mail: jschmitt@hs.uni-hamburg.de).

Conical dislocations in crumpling

Enrique Cerda*, Sahraoui Chaieb†, Francisco Melo* & L. Mahadevan†

** Departamento de Física de la Universidad de Santiago de Chile, Avda Ecuador 3493, Casilla 307 Correo 2, Santiago, Chile*
† Department of Mechanical Engineering, Massachusetts Institute of Technology, 77 Massachusetts Avenue, Cambridge, Massachusetts 02139, USA

A crumpled piece of paper is made up of cylindrically curved or nearly planar regions folded along line-like ridges, which themselves pivot about point-like peaks; most of the deformation and energy is focused into these localized objects. Localization of deformation in thin sheets is a diverse phenomenon[1–6], and is a consequence of the fact[7] that bending a thin sheet is energetically more favourable than stretching it. Previous studies[8–11] considered the weakly nonlinear response of peaks and ridges to deformation. Here we report a quantitative description of the shape, response and stability of conical dislocations, the simplest type of topological crumpling deformation. The dislocation consists of a stretched core, in which some of the energy resides, and a peripheral region dominated by bending. We derive scaling laws for the size of the core, characterize the geometry of the dislocation away from the core, and analyse the interaction between two conical dislocations in a simple geometry. Our results show that the initial stages of crumpling (characterized by the large deformation of a few folds) are dominated by bending only. By considering the response of a transversely forced conical dislocation, we show that it is dynamically unstable above a critical load threshold. A similar instability is found for the case of two interacting dislocations, suggesting that a cascade of related instabilities is responsible for the focusing of energy to progressively smaller scales during crumpling.

To probe volume-restricting deformations that lead to localization in a simple setting, we consider a circular sheet of diameter $2R_p$ that is forced axially by a distance d into a rigid cylindrical hoop of diameter $2R < 2R_p$, in a manner similar to pushing coffee-filter paper into a funnel (Fig. 1). Owing to the energetically prohibitive

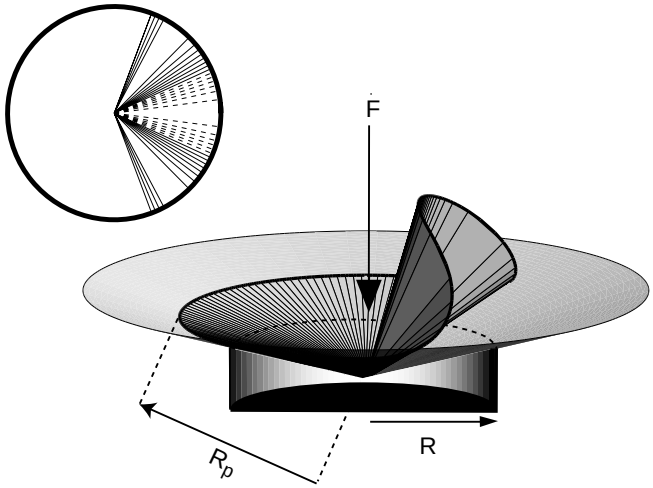

Figure 1 Geometry of an ideal conical dislocation. The shape is computed by solving the Euler–Lagrange equations corresponding to minimizing $L(\psi)$ in equation (1), with $\epsilon = 0.365$. The figure also shows the parameters that are experimentally controllable: R, the radius of the support; R_p, the radius of the sheet (depicted as a ruled surface); and the transverse applied force, F. At top left we show the generators of the conical surface: the solid lines correspond to the negatively curved region (concave-up) and the dotted lines correspond to the positively curved region.

requirement of making an axisymmetric cone, the sheet deforms into a non-axisymmetric conical surface that is in partial contact with the hoop[10,11]. This surface has a single plane of symmetry and is isometric to the plane everywhere except near its tip or core; that is, it is a near-perfect developable cone[5,12]. Only in the vicinity of the tip is the sheet stretched appreciably; elsewhere it is bent without stretching. This surface is also a rotational edge-dislocation, or conical dislocation, according to the Volterra classification[11,13] and affords the simplest example of strain localization.

As this conical surface is nearly developable, its geometry can be characterized in terms of its generators[14] away from the tip. These generators are most easily viewed using light reflected from the surface of a painted sheet that is illuminated with linearly polarized light incident along the axis of deformation. When viewed through a cross-polarizer, this leads to images such as that shown in Fig. 2. Away from the tip, the isochromatic lines (along which there is no radial curvature) are straight and form the generators of the perfect developable cone[11]; close to the tip, they have a well defined radius of curvature R_c, that characterizes the size of the core where there is appreciable stretching. We determine R_c by fitting a parabola to the curved isochromatic line passing through the core. In Fig. 3a, we plot R_c as a function of the deformation characterized by $\epsilon = d/R$. The data are best fitted by two power laws; for $\epsilon \leqslant 0.1$, $R_c \propto \epsilon^{-0.33\pm0.01}$, while for $\epsilon \geqslant 0.1$, $R_c \propto \epsilon^{-0.50\pm0.02}$.

To understand these results, we consider the deformation of a circular sheet into a conical surface using eulerian coordinates. We let (ρ, θ) be the polar coordinates of a point in the horizontal plane defined by the edge of the supporting hoop, so that the vertical displacement of the sheet is $\rho\psi(\theta)$ where $\psi(\theta)$ is the tangent of the angle between a generator of the surface and the horizontal. In the deformed state, the sheet is in partial contact with the hoop so that it fits inside the axisymmetric envelope cone $z = \rho\epsilon$. If the sheet is very thin and the deformations are moderate ($\epsilon \leqslant 0.4$), the irreversible plastic deformation near the tip is small. Therefore we can use the theory of elasticity to describe its shape reasonably well. Away from the core the developable cone $\rho\psi(\theta)$ is determined by minimizing the bending energy subject to the constraints due to inextensibility and contact. Generalizing the functional given in ref. 11 to account for possibly large curvatures of the sheet requires the minimization of the following functional for $\psi(\theta)$:

$$L(\psi) = U_b + \lambda\int_{-\pi}^{\pi}\left[1 - \frac{(1+\psi^2+\psi'^2)^{1/2}}{1+\psi'^2}\right]d\theta + \int_{-\pi}^{\pi} b(\theta)(\epsilon-\psi)d\theta \quad (1)$$

Here $U_b = (E_b/2)\ln(R_p/R_c)\int_{-\pi}^{\pi}[(\psi+\psi'')^2(1+\psi^2)^2]/(1+\psi^2+\psi'^2)^{5/2}\,d\theta$ is the bending energy, and E_b is the bending stiffness. The second term on the right enforces the inextensibility constraint and λ is proportional to the hoop stress. The third term enforces the requirement that the deformed sheet lies inside the perfect cone $z = \rho\epsilon$, with $b(\theta) = 0$ when $\psi \geqslant \epsilon$, and $b(\theta) \geqslant 0$ when $\psi = \epsilon$, and $b(\theta)$ related to the normal reaction of the supporting hoop on the conical dislocation. Figure 1 shows a numerically computed shape of the developable cone accounting for large bending deformations, and yields a solution valid everywhere except in the neighbourhood of the tip where the effects of stretching cannot be neglected.

We now estimate the core size characterized by the radius R_c which results from a balance between the bending and stretching energy. In the core of area ΔS, the stretching energy is $U_s \approx E_s\gamma^2\Delta S$, where γ is the in-plane strain and E_s is the stretching stiffness. The bending energy in the core is $U_b \approx E_b\kappa^2\Delta S$ where κ is the mean curvature in the core[15]. Equating these energies yields $U_b/U_s \approx (E_b/E_s)(\kappa/\gamma)^2 \approx O(1)$. The stretching strain can be estimated from the change in length of a typical generator of length R, the scale over which forces and torques are exerted. This generator is stretched to a length $\sqrt{R^2+\epsilon^2R_c^2}$: then the strain is $\gamma \approx (\sqrt{R^2+\epsilon^2R_c^2} - R)/R \approx (\epsilon R_c/R)^2$. The bending strain is simply the mean curvature κ which we now estimate. When $\psi, \psi' \ll 1$, $U_b \approx \kappa^2 \approx \psi^2 \approx \epsilon^2$, while when $\psi, \psi' \gg 1$, $U_b \approx \kappa^2 \approx \psi^2\psi'^4/\psi'^5 \approx \epsilon$ (E.C. and L.M., manuscript in preparation). Therefore for small deformations, $\kappa \approx \epsilon/R_c$, while for large deformations, $\kappa \approx \epsilon^{1/2}/R_c$. This cross-over in the scaling occurs due to the change in the geometry of the sheet as ψ, ψ' are small or large compared to unity, so that the curvature (and the force) changes in response to it. Substituting in these strains into the energy balance yields the scaling law

$$R_c \approx \left(\frac{E_b}{E_s}\right)^{1/6}\epsilon^{-p}R^{2/3}; \quad p = \begin{cases} 1/3, & \epsilon \ll 1, \\ 1/2, & \epsilon \approx O(1) \end{cases} \quad (2)$$

consistent with the experimental results shown in Fig. 3a. This relation is valid for thin sheets of arbitrary materials subjected to large deformations, and extends the results obtained for the weak deformations of ridges[8]. The first factor in the scaling law is associated with material properties; for an isotropic material $E_b/E_s \approx h^2/(1-\nu^2)$, where h is the sheet thickness and ν is Poisson's ratio. The second arises from the geometry of deformation as ϵ characterizes the cone angle. This factor also hides a subtle dependence on the force $F = \partial U_b/R\partial\epsilon$ since the force–deflection relation, discussed later, is of the form $\epsilon = \nu(FR/E_b)$, where $\nu(s)$ is a dimensionless function. There is also a logarithmic dependence on the sheet radius R_p but it is difficult to detect experimentally. The third factor characterizes the length R associated with the moment arm of the reaction force along the hoop.

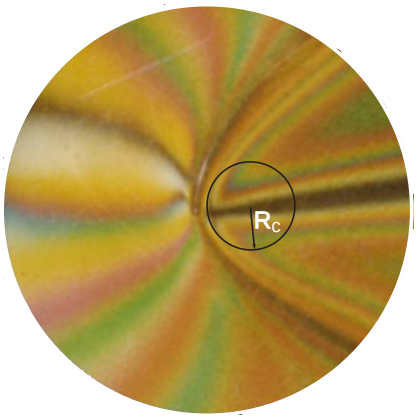

Figure 2 Geometry of a real conical dislocation. Cross-polarizers are used to view the reflected light from a painted sheet deformed into a conical dislocation. Isochromatic lines correspond to lines with no radial curvature, and coincide with generators of the cone away from the tip. In the core of the dislocation close to the tip, the sheet stretches into a surface of double curvature. Here the isochromatic lines have a radius of curvature R_c.

Next we consider the behaviour of the conical dislocation when a force F is applied along the axis of the supporting hoop. In our experiments, a round tip of diameter 0.5 mm is attached to a load control cell which is used to measure the applied force. Care is taken to minimize frictional effects by lubricating the contact zone between the sheet and supporting hoop. We restrict our range of deformations to minimize inelastic effects. In Fig. 3b we plot F versus ϵ and see that for $\epsilon \leqslant 0.1$, $F \propto \epsilon$ but for $\epsilon \geqslant 0.1$ $F \approx \epsilon^p$, $p < 1$. The location of this cross-over coincides with that in Fig. 3a for the cross-over in the scaling law for R_c, suggesting that it is geometric effect. As ϵ increases, the effective reaction force from the hoop, which is normal to the sheet in the absence of friction, starts to become more horizontal, while the torque increases. This decreases the resistance to further deformation and softens the system, eventually leading to an instability. We quantify this by evaluating F in terms of the bending energy U_b, $F = \partial U_b/\partial d = (E_b/R)\ln(R_p/R_c)\partial u(\epsilon)/\partial\epsilon$. Here $u(\epsilon)$ is a dimensionless function such that $u \approx \epsilon^2$ for small ϵ and $u \approx \epsilon$ for large ϵ, following an argument identical to that for the scaling of the curvature. We use

experimentally determined values of R_p and E_b for each material, and the linear part of the experimental curve to estimate R_c. A numerical method is used to solve the boundary-value problem associated with the Euler–Lagrange equations that arise from minimizing the functional $L(\psi)$ in equation (1). We use the analytical solution determined in ref. 11 as an initial guess for small ϵ and then use an iterative procedure to determine the complete $F-\epsilon$ curve shown in Fig. 3b. The experimental data are well explained by our theory that accounts only for bending, and indicate that stretching is not important in this case. Continuing this computation beyond the experimentally determined points, we find that the stiffness of the system eventually goes to zero, signifying a subcritical (snap-through) dynamic instability in a force-controlled experiment[16] that is arrested when the sheet contacts itself.

So far we have described the structure and the response of a single centrally forced sheet that leads to a conical dislocation with a fold that is rotation-invariant. In the course of crumpling, two such dislocations often interact with each other, forming ridges that break this rotation symmetry. Prior studies[8] have focused on the structure and linear response of these ridges, artificially excluding the effects of the conical dislocations that they connect. We now consider them explicitly in the context of an experiment by forcing an acetate sheet into a circular hoop at two non-central locations. The two probes lie on a diameter and are separated by a distance $2D$, so that we have an additional control parameter $\delta = D/R$. As the probes are moved axially by a distance d, two conical dislocations appear at symmetrical locations with respect to the centre of the hoop. In Fig. 4a we show one such configuration, computed by solving the Euler–Lagrange equations obtained by minimizing $L(\psi)$ in equation (1). This solution minimizes the bending energy of the sheet but does not account for stretching, so that it leads to a flat interlying region instead of a stretched ridge in between the dislocations. To compare these calculated results with experiment, we consider the mechanical response of this structure characterized by a $F-\epsilon$ curve, shown in Fig. 4b. The theoretical curve has no tunable parameters, and shows that bending alone accounts very well for the measured force. To quantify this further, we recall that the stored bending energy in this structure is $U_b = E_b f(\delta,\epsilon)\ln(R_p/R_c)$, with $f(\delta,\epsilon) \approx 84.7\epsilon^2(1+\text{const.}\delta)$ for

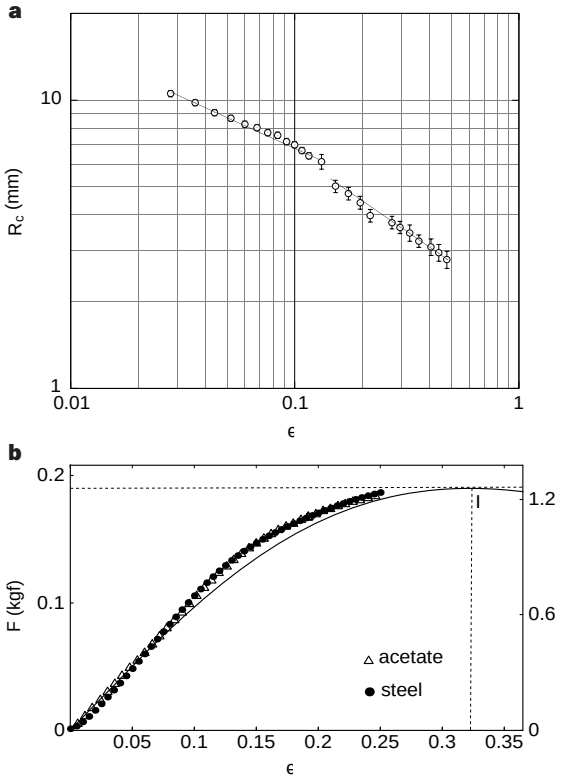

Figure 3 Mechanical response of a conical dislocation. **a**, The core size R_c as a function of the deformation of the conical dislocation characterized by $\epsilon = d/R$. In our experiments we used a series of thin sheets of steel (bending stiffness $E_b = 7.76\times10^{-3}$ N m, thickness $h = 0.075$ mm) and acetate (bending stiffness $E_b = 5.1\times10^{-4}$ N m, $h = 0.1$ mm). The radii of the sheets varied from 15 to 90 mm, while the radius of the supporting hoop was 5 mm less than the radius of the sheet. The transverse displacement d of the centre of the thin sheet relative to the plane of the hoop is measured using a precision micrometer with an accuracy of 10 μm. The data are best fitted by the power laws $R_c \propto \epsilon^{-0.33\pm0.01}$, $\epsilon \leqslant 0.1$, $R_c \propto \epsilon^{-0.50\pm0.02}$, $\geqslant 0.1$ (solid lines). The jump in the data at $\epsilon \approx 0.1$ corresponds to using two different hoop sizes. The error bars are larger as ϵ increases due to a decrease in the core size which leads to having fewer data points. **b**, The force–deformation curve for a conical dislocation made of acetate (open triangles; left ordinate) and steel (filled circles; right ordinate), compared with the theoretical curve (solid line) calculated using the expression for the force F given in the text, with no adjustable parameters. We ascribe the small systematic overshoot of the experimental data to frictional effects. The maximum l in the theoretical curve corresponds to the location of a subcritical (snap-through) instability in a force-controlled experiment.

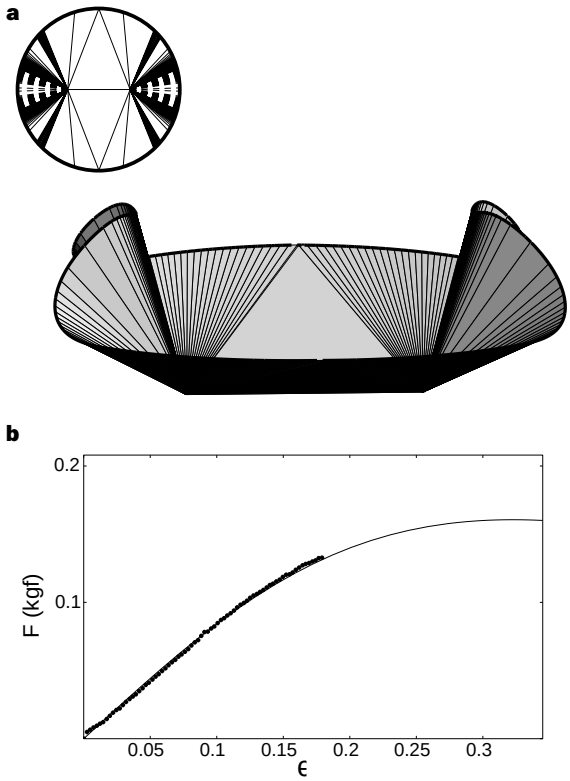

Figure 4 Geometry and mechanical response of two interacting conical dislocations. **a**, When a sheet is forced transversely into a rigid circular hoop at two locations along a diameter, it deforms into a boat-like structure with two symmetrically placed conical dislocations. This solution with least energy is calculated by solving the Euler–Lagrange equations that arise from minimizing $L(\psi)$ in equation (1), starting with an analytical solution for two weakly deformed conical dislocations with $\delta = D/R = 0$, $\epsilon = d/R \ll 1$, and using an iterative continuation scheme until $\delta = 0.38$, $\epsilon = 0.345$. This solution accounts only for the effects of bending, and the associated generators are shown at top left. The diamond-shaped region between the dislocations consists of two flat planes, and is separated from the conical regions by lines along which the curvature of the sheet suffers a discontinuity. Accounting for stretching and bending will lead to boundary layers at these locations. **b**, The force–deformation curve for two interacting conical dislocations in an acetate sheet, compared with the theoretical curve (solid line), with no adjustable parameters. We see that a theory accounting for bending alone is able to explain the response of this structure which exhibits a sub-critical instability for moderate ϵ, as evidenced by the presence of a maximum in the $F-\epsilon$ curve.

small ϵ, δ while the energy which resides in the stretched ridge[8] is $U_s = E_b\epsilon^{7/3}(2D/h)^{1/3}$, so that $U_s/U_b \approx 0.05$ for typical experimental parameters. These results indicate that in the early stages of crumpling, when large deformations of a few conical dislocations are much more likely to occur, bending dominates stretching. Finally, by continuing the computation of the $F - \epsilon$ curve beyond the experimentally accessible parameters, we see the appearance of a snap-through instability similar to that for a single dislocation.

A series of such events (that is, geometric softening—dynamic snap-through—local topological stiffening) provides us with a microscopic mechanism for the crumpling of a large thin elastic sheet. As the sheet is deformed by a force, it forms a developable cone that deforms, softens and eventually becomes dynamically unstable, and an acoustic pulse is emitted when the sheet pops into a folded configuration. This stiffens the sheet locally, but soon new developable cones (and stretched ridges which connect them) begin to form. Ridges may buckle in two ways. (1) In the plane of the ridge by forming a developable cone about which the ridge pivots and folds, locally leading to roughly the same scenario as that for a single conical dislocation, or (2) in a direction perpendicular to the ridge by forming two dislocations that move apart along a new ridge about which the original ridge folds, as seen during the bending of a drinking straw. A cascade of these instabilities on ever-decreasing length scales leads to the formation of new conical dislocations as the sheet crumples, and the energy of deformation is pumped down to smaller and smaller scales. As the size of these folds becomes smaller, the incremental deformation is concomitantly less, and a cross-over to the regime where stretching and bending deformations are of the same order is likely[8]. However any analysis of this stage in crumpling must also account for inelastic deformations. On length scales much larger than the thickness but much smaller than the length or breadth of the sheet, these dynamical snap-throughs constitute a self-similar cascade and are accompanied by acoustic emissions. While preliminary experiments[17,18] are suggestive of power-law behaviour for the statistics of these sounds, they remain incompletely quantified: much work remains to be done in this area. □

Received 1 February; accepted 17 June 1999.

1. Calladine, C. *Theory of Shell Structures* (Cambridge Univ. Press, Cambridge, 1983).
2. Wierzbicki, T. & Jones, N. (eds) *Structural Failure* (Wiley Interscience, New York, 1988).
3. Connelly, R. Rigidity and energy. *Invent. Math.* **66,** 11–33 (1982).
4. Nelson, D. R., Piran, T. & Weinberg, S. *Statistical Mechanics of Membranes and Surfaces* (World Scientific, Singapore, 1988).
5. Amirbayat, J. & Hearle, J. W. S. The complex buckling of flexible sheet materials. *Int. J. Mech. Sci.* **28,** 339–370 (1986).
6. da Vinci, Leonardo *Notebooks* Vol. I., *Studies of Drapery* (Dover Reprint, New York, 1984).
7. Rayleigh, Lord, *Theory of Sound* Vol. I, Ch. X a (Dover, New York, 1945).
8. Lobkovsky, A., Gentges, S., Li, H., Morse, D. & Witten, T. Stretched ridges in crumpling. *Science* **270,** 1482–1485 (1995).
9. Lobkovsky, A. & Witten, T. A. Properties of ridges in elastic membranes. *Phys. Rev. E* **55,** 1577–1589 (1997).
10. Chaieb, S. & Melo, F. Experimental study of developable cones. *Phys. Rev. Lett.* **80,** 2354–2357 (1998).
11. Cerda, E. & Mahadevan, L. Conical surfaces and crescent singularities in crumpled sheets. *Phys. Rev. Lett.* **80,** 2358–2361 (1998).
12. Ben Amar, M. & Pomeau, Y. Crumpled paper. *Proc. R. Soc. Lond. A* **453,** 729–755 (1997).
13. Nabarro, F. R. N. *Theory of Crystal Dislocations* (Dover, New York, 1993).
14. Struik, D. J. *Lectures on Classical Differential Geometry* (Dover, New York, 1988).
15. Love, A. E. H. *A Treatise on the Mathematical Theory of Elasticity* (Dover, New York, 1944).
16. Timoshenko, S. & Gere, J. *Theory of Elastic Stability* (McGraw-Hill, New York, 1961).
17. Kramer, E. & Lobkovsky, A. Universal power law in the noise from a crumpled elastic sheet. *Phys. Rev. E* **53,** 1465–1468 (1996).
18. Houle, P. & Sethna, J. Acoustic emission from crumpling paper. *Phys. Rev. E* **54,** 278–283 (1996).

Acknowledgements

E.C. was supported by the Chilean Presidente de la República postdoctoral fellowship during the course of this work at MIT in 1997–98. S.C. was supported by a postdoctoral fellowship at Universidad de Santiago de Chile in 1997–98 during the course of this work. Additional support was provided by the Chilean Cátedra Presidencial en Ciencias (F.M.), the Karl van Tassel career development chair and the Sloan fund (L.M.) at MIT.

Correspondence and requests for materials should be addressed to L.M. (l_m@mit.edu).

Direct observation of *d*-orbital holes and Cu–Cu bonding in Cu_2O

J. M. Zuo*, M. Kim*, M. O'Keeffe† & J. C. H. Spence*

* *Department of Physics and Astronomy,* † *Department of Chemistry, Arizona State University, Tempe, Arizona 85287, USA*

A striking feature of metal oxide chemistry is the unusual electronic and chemical behaviour of Cu(I) and Ag(I): a case in point is that detailed understanding of Cu–O bonding is essential to the theory of high-temperature copper oxide superconductors. Both cations are usually coordinated in a linear fashion to two oxygens, particularly for Cu(I). In many compounds, the Cu(I) and Ag(I) cations also adopt close-packed (and related) configurations with short metal–metal distances that are strongly suggestive of the occurrence of metal–metal bonding[1,2] despite their formal nd^{10} configuration. Such observations have been explained[3,4] by invoking the participation in bonding of electronic orbitals of higher principal quantum number—that is, $(n+1)s$ and $(n+1)p$—accompanied by the creation of *d*-orbital holes on the metal ion. To test this hypothesis, we have used a recently developed method of quantitative convergent-beam electron diffraction[5] combined with X-ray diffraction to map the charge-density distribution in the simple oxide Cu_2O, the results of which we then compare with electronic-structure calculations. We are able to image directly the *d* holes on the copper atoms, and also demonstrate the existence of Cu–Cu bonding in this compound.

Cu_2O has a cubic structure with no free internal parameters (only Ag_2O is isostructural). The copper atoms are at the points of a face-centred-cubic lattice, with oxygen atoms in tetrahedral sites at positions (1/4,1/4,1/4) and (3/4,3/4,3/4) of the cubic cell. The resulting arrangement of Cu–O links is made up of two interpenetrating networks (Fig. 1). The simplest description of Cu_2O using an ionic model with closed-shell (spherical) Cu^+ and O^{2-} ions is known to be inadequate. Not only does it fail to explain the observed linear 2-coordination of Cu but also it is not in accord with the observation that the two sublattices repel each other electrostatically, so that to account for their interpenetration some short-range Cu–Cu attractive interaction must be invoked[6]. We note that the closest approach of atoms of the two networks is a Cu–Cu distance of 3.02 Å—the shortest O–O distances are 3.70 Å.

Considerable progress has been made in mapping the charge density of light-element molecular crystals by X-ray diffraction[7], especially using a synchrotron source[8]. The extension of this method

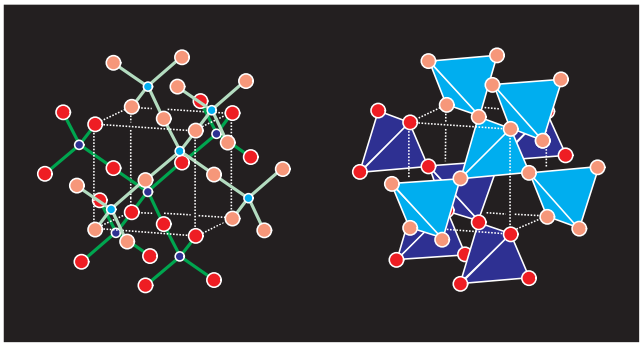

Figure 1 The structure of Cu_2O. Left, as a ball and stick model with O atoms blue, Cu atoms red and bonds green. One network is coloured darker than the other. Note that there are no bonds joining the two nets. Right, as corner-connected OCu_4 tetrahedra. Dark and light tetrahedra are on independent networks. In both sketches, dotted white lines outline a unit cell.